Long-term Deformation Mechanism of Masjed-e-Soleyman High Rockfill Dam

Morteza Salari[1], Ali Akhtarpour[2*], Sajjad Khosravi[3,4]

[1] Department of Civil Engineering, Faculty of Engineering, Ferdowsi University of Mashhad, Iran

Email Address: m.salari04@gmail.com

Tel: +989156499714

[2] Department of Civil Engineering, Faculty of Engineering, Ferdowsi University of Mashhad, Iran

[*]Corresponding author. Email address: akhtarpour@um.ac.ir

Orcid.org/0000-0003-1654-0194

Tel: +989153143978

[3] Department of Civil Engineering, Iran University of Science and Technology, Iran

Present address [٤]: Department of Geotechnical Engineering, School of Civil Engineering, Iran University of Science and Technology, Tehran 16846-13114, Iran.

Email Address: geo.sajad.406@gmail.com

Tel: +989398017427

Orcid.org/0000-0002-4834-342X

Abstract

The Masjed-e-Soleyman dam, situated in southern Iran, is a rock-fill dam with a clay core, reaching a height of 178 meters. During the construction and impounding phases, notable pore water pressure was developed within the core. The dissipation rate of this pressure is considerably slow, persisting long after impounding. Nonetheless, progressive deformations and irregularities have been observed and documented on the

surface of the dam's body, with no significant decrease in the rate of deformation. These deformations have raised concerns regarding the safety and stability of the superstructure. This study aims to investigate all factors influencing such deformation behavior by analyzing instrumental data and employing a mechanical-fluid three-dimensional numerical model. A modified softening-hardening constitutive model is utilized to simulate the phenomena of rock-fill particle crushing and saturated collapse within the upstream rock-fill shell materials. Additionally, a viscoelastic creep model is employed to simulate creep deformations. Subsequently, a robust hypothesis concerning the long-term mechanism of dam deformation behavior is formulated. According to this hypothesis, the main contributors to the complex behavior of this dam are the creep deformations of the rock-fill shell and the clay core's deformation under constant volume conditions.

Keywords: High rock-fill dams ،Softening-Hardening constitutive model ،Particle Breakage ،Collapsed settlement ،Creep

1. Introduction

Rock-fill materials are commonly used in the construction of dams, sourced either from river beds with rounded or sub-rounded aggregates or from rock borrow zones where sharp-edged aggregates are obtained through blasting. These materials have been extensively employed in the construction of rock-fill dams [1, 8]. Large-scale triaxial tests are commonly performed to assess the strength and deformation characteristics of rock-fill materials [9, 11]. Various constitutive models, including the non-linear elastic model [12], the elastoplastic hardening model [13], and the strain softening elastoplastic model [14], can be utilized to predict the mechanical behavior of granular materials. While linear or non-linear elastic models were previously common in simulating rock-fill behavior [15], the use of sophisticated constitutive elastoplastic

models based on the disturbed state idea [16] and the critical state concept [17] has become more prevalent.

Collapse behavior has been observed in numerous geotechnical materials based on laboratory research and field observations [18, 23]. In the case of clay-core rock-fill dams, settlement in the upstream shell can lead to increased settlement of the rock-fill shell compared to the core during the initial impounding phase. For instance, the upstream shell of the Cherry Valley dam settled four times more than the central core, resulting in longitudinal cracks on the crest and the shell-core interface [24]. Various methods have been proposed to model collapse settlement. Nobari and Duncan introduced a method that directly applies triaxial test results and is based on the hyperbolic model proposed by Duncan and Chang [12]. Another approach developed by Naylor et al. integrates the methods of Nobari and Duncan and employs a critical state elastoplastic model [25]. The Naylor technique has been applied to simulate collapse and settlement in the Beliche Dam with a rock-fill shell. Other approaches incorporate frameworks from unsaturated soil and porous medium mechanics [26]. In the context of saturated soil mechanics, Mahinroosta and Alizadeh [27] developed a method for simulating collapse settlement using a hardening/softening constitutive model. This technique was applied to model the collapse settlement of the rock-fill shell in the Gotvand Dam [28]. The effectiveness of this technique in replicating the collapse settlement of the rock-fill shell in the Masjed-e-Soleyman Dam was investigated by Akhtarpour and Salari [2].

Long-term deformation records of the Masjed-e-Soleyman Dam in southwest Iran reveal significant creep behavior in its rock-fill structure. Despite the stress state remaining unchanged, the dam continues to deform long after its completion [29]. This macroscopic creep behavior can be attributed to the subcritical propagation of cracks

within stressed particles [30]. Extensive laboratory and in-situ experiments have been conducted to study the creep behavior of rock-fill materials [31, 32] and rocks [33, 34]. The findings suggest that rock-fill creep, characterized by continuous crushing, is influenced by various factors such as rock type, mineralogical composition, grain size distribution, stress state at grain contacts, initial density, particle characteristics, moisture content, time-dependent degradation of solid hardness due to chemical reactions, and environmental factors like temperature and freeze-thaw actions. Based on these experimental findings, several constitutive models have been proposed, employing a continuum approach that relates time to long-term strain through a logarithmic relationship [35].

The Masjed-e-Soleyman Dam is a 178-meter high rock-fill dam with a central core. Despite extensive research [2], the long-term deformation behavior of this dam remains complex and challenging to fully understand. Instrumentation records show significant pore water pressure during construction and initial impounding, which dissipates very slowly, taking about 14 years. Although minimal consolidation-induced deformation in the core was expected, the dam body has exhibited substantial and continuous deformations, including significant subsidence of the crest, longitudinal berm-like subsidence on the upstream surface, and extensive tensile cracks near the crest and abutments. These ongoing deformations pose concerns about the long-term safety and stability of the structure.

The rock-fill shells of the dam consist of conglomerate with calcareous cement components. Previous studies have demonstrated that the strength and deformation behavior of rock-fill materials are influenced by particle size distribution, rotation, particle breakage, and re-arrangement. These factors have contributed to notable subsidence in the upstream shell of the dam caused by saturation during the initial

impounding, as well as long-term creep deformations in the rock-fill shell [2]. In this study, by analyzing data obtained from the dam instrumentation system and employing three-dimensional numerical simulations, the primary causes underlying its complex deformation behavior are identified, and the most plausible hypothesis is presented.

2. Masjed-e-Soleyman dam (MES Dam)

The Masjed-e-Soleyman Dam, previously known as "Godar-e-Landar," is a rock-fill dam located on the Karun River in southwest Iran. It has a reservoir capacity of 261 million cubic meters and generates 2000 MW of electricity. The primary cross-section of the dam, has a crest length of 500 meters and a width of 15 meters. The surrounding rock mass consists of alternating layers of siltstone and conglomerate from the Aghajari and Bakhtyari formations. The dam was constructed in a narrow valley with wall slopes averaging 36 degrees.

Site evaluations identified the Simband borrow area as the ideal source of materials for the dam's core. The borrow area contains layers of clay (CL) and clayey gravel (GC) distributed irregularly. The upper one-third of the core was compacted with a water content below the optimum level, while the lower two-thirds were compacted with a water content exceeding the optimum level. The dam's shells are made of compressed conglomerate rock fill obtained through blasting, with insufficient moisture content. Regions 3A and 3C have coarser aggregates compared to area 3B. Properly graded conglomerate aggregates are present in the filter zones (2A, 2B, and 2C).

To monitor stress, pore pressure, and settlement within the dam, various instruments were strategically positioned at chainages (CH.) 160, 260, 360, and 420 meters from the left side of the crest's end. However, significant deformations during the final 50 meters of embankment construction damaged many of these instruments, including Electrical Piezometers (EP), Total Pressure Cells (TPC), and magnetic plates (MP). At

CH. 260 in the primary cross-section (Fig. 1-Supplementary), the instruments remained intact. Each cluster (C) in this cross-section includes three horizontally installed TPCs tilted at 45 degrees upward and 45 degrees downward, along with a single EP. Additionally, a system of survey measurement points (SMP) was established on the dam to monitor surface displacements approximately one month after the first impounding began, when the water reservoir level had risen by around 57 meters (refer to Fig. 2- Supplementary).

3. Dam Monitoring during a long-term period

During the construction of the Masjed-e-Soleyman Dam, the generated fill load increased vertical stress, causing elevated excess pore water pressure and deformation. The first impounding introduced water pressure on the core and foundation, with buoyancy forces and saturation collapse occurring in the upstream shell due to water ingress [36]. Significant excess pore water pressure was observed during construction, mainly due to the rapid construction rate and low permeability of the core. Minor changes in the pore water pressure ratio (PWP) over time suggest minimal dissipation of excess pressure even 14 years after impounding.

The core's permeability decreases exponentially with increased effective vertical stress, leading to long-term dissipation of excess pore pressure, especially near the filters [2]. In the lower parts of the core, the PWP and stress ratios (r_u and r_k) approach unity, indicating a quasi-fluid behavior due to high excess pore water pressure and almost incompressible conditions.

After the completion of the initial impounding of the Masjed-e-Soleyman Dam, significant rotations in the direction of the principal stresses were observed in the main cross-section. Above level 270, the stresses rotated anti-clockwise, while below level 230, a clockwise rotation was noted, reflecting complex stress behaviors. Shear

movements in the dam were associated with contractive behavior, influencing the overall stability of the structure.

Measurements from magnetic plates (MPs) and survey points indicated notable deformations. For instance, during construction, the core experienced a maximum settlement of 3.7 meters, a behavior that contrasts with the expected slow consolidation characteristic of the core. Additional settlements of up to 2.2 meters were observed at the crest during the initial impounding, primarily driven by high excess pore water pressure rather than consolidation.

The SMP was installed one month after the first impounding to assess surface displacements. Half of the total settlement occurred during the initiation of the first impounding, with settlements in the upstream shell being a significant factor influencing the deformation behavior during the first impounding. The temporal variation in settlement and horizontal displacement (perpendicular to the dam axis) of surface measurement points, situated in the maximum cross-section of the dam, are illustrated in Fig. 1 and 2 (Fig. 1- Supplementary and 2- Supplementary show the corresponding locations). As reported by Hunter (2003) [24] in regards to surface deformations observed in rock-fill dams during the post-construction phase (Fig. 3), the SMP21 benchmark is situated in zone three, which experiences the most significant impact from deformations in the upstream shell. Similarly, SMP22, located in region two, is primarily influenced by deformations in the core. Fig. 1 and 2 demonstrate a nearly identical magnitude and rate of deformations at these two points, signifying a similar deformation behavior for the dam core and the upstream shell at upper elevations. Over a period of 14 years since the commencement of impoundment, the deformations within these regions exhibit an increasing trend. Remarkably, the maximum settlement recorded on the dam surface, since the conclusion of

impoundment, amounts to 3.01 meters in these areas. It is important to note that these deformations are unrelated to the consolidation mechanism due to the negligible dissipation of excess pore pressure within the core.

On the downstream surface, the deformations at SMP23 and SMP24, located respectively at heights of 0.8 and 0.6 within the primary section of the dam, are more influenced by deformations in the downstream rock-fill shell. While these points demonstrate the highest horizontal displacements (1.3 m) since the end of impounding, their settlements are one-third of those observed at crest points. Given that the dam shell consists of rock-fill materials, it is the phenomenon of creep that governs their long-term deformation behavior. Consequently, creep deformations in the shell materials play a crucial role in the long-term deformation mechanism of the dam.

SMP25, located in the lower portion of the dam shell, is most susceptible to deformations originating from the dam foundation. However, the deformation at this point is minimal, as depicted in Fig. 2. In order to assess the deformation characteristics of the underlying rock foundation, a series of measurement points were installed inside the dam inspection gallery, situated on the rock foundation below the core and dam axis, in 2010, eight years after the initial impoundment. The variation of surface settlement from early 2010 to 2015 is presented in Fig. 4. The maximum settlement recorded within the inspection gallery (on the rock) over a period of approximately five years amounted to 7 mm, while during the same timeframe, the settlement at the crest point (SMP21) reached approximately 1.5 meters (see Fig. 1). Additionally, in January 2006, a set of in-place electrical inclinometers (INC) was installed at the main section of the dam downstream of the core through drilling operations to evaluate the deformation interaction between the shell, core, and foundation. The location of this

inclinometer and the profiles of horizontal displacement recorded since installation are shown in Fig. 5. It is evident that the magnitude of lateral deformations at levels adjacent to the foundation is negligible and increases with height. Based on these observations, it can be concluded that the deformations in the foundation of the MES dam are minimal compared to those exhibited by the dam body, indicating that the foundation does not exert a decisive influence on the long-term deformation mechanism of the dam. On the contrary, the increase in lateral deformations with increased height confirms that creep phenomenon in rock-fill shells can significantly impact the dam's long-term deformation behavior.

4. Numerical modeling

The investigation of dam behavior was conducted through three-dimensional modeling using the FLAC 3D program, as illustrated in Fig. 6. The modeling employed the finite difference method, utilizing 75,600 hexahedral tetrahedral elements. In order to ensure modeling accuracy, the dimensions of element edges, model dimensions, and geometric boundaries of the lateral and bottom aspects of the numerical model were selectively chosen to avoid impacting the modeling results. The analysis encompassed the simultaneous consideration of flow-mechanical formulation. Specifically, consolidation in the core, collapse in the upstream rock-fill material, and creep in the upstream and downstream rock-fill material were taken into account during the construction period, first impoundment, and long-term period, respectively.

During the initial impounding and construction phases, the mechanical behavior of materials was simulated using the elastoplastic hardening/softening constitutive model (See Appendix). This constitutive model implements the elastic modulus based on the Duncan and Chang equation [12], which has been validated by numerous researchers (2020). Frictional hardening and dilatancy behavior were simulated using the modified

equation proposed by Vermeer and de Borst [37], as well as the modified equation proposed by Rowe [38] and further modified by Akhtarpour and Salari [2].

In order to obtain parameters for the modified constitutive model used in the dam materials, conventional triaxial tests were conducted on core samples. Additionally, large-scale triaxial tests were performed at Karlsruhe University on the coarse-grained materials found in the shell, filter, and drainage regions of the dam [2].

To determine the parameters of the materials used in the dam body, conventional and large-scale triaxial tests were simulated using the FLAC software platform. The constitutive model was implemented with all relevant functions and equations using the FISH programming language within the software. The simulations utilized a single element with axial symmetry and appropriate boundary conditions. During each stage of analysis, the program calculated the plastic shear strain and updated the model parameters based on the defined functions and equations. (For calibration details under diverse conditions see Fig. 3- Supplementary)

The final parameters are presented in Table 2. In this analysis, the cohesion value is determined based on the distance between the origin of the tangent line and Mohr's circles. As presented in Table 2, the exponent (n) for regions 3A and 3C under initial dry conditions exhibits a negative value, indicating that an increase in confining stress causes a decrease in Young's modulus. These regions, characterized by more extensive breakage compared to others, display the highest values of I_d. The fine-grained nature of the core materials poses challenges for breakage, resulting in an I_d value of 1 for these materials.

The surrounding rock mass was modeled using a linear elastic constitutive model, and the corresponding parameters can be found in Table 3. The FLAC3D software [39]

employed a flow-mechanical formulation that incorporates a permeability function dependent on the effective vertical stress, as proposed in Eq. 1.

$$K_{\mathrm{int}(y)} = \begin{cases} 2\times10^{-8} & \dfrac{K_{\mathrm{int}(x)}}{K_{\mathrm{int}(y)}} = 2.5 \\ 1.82\times10^{-6}\left(\dfrac{\sigma_y^{'}}{P_a}\right)^{-0.48} & \end{cases} \qquad \text{Eq.1}$$

Where $K_{int(x)}$ and $K_{int(y)}$ are the horizontal and vertical saturated permeability coefficients (cm/s), and σ'_y is the effective vertical stress (*kPa*).

After the initial impounding, the mechanical response of the rock-fill materials was analyzed employing a visco-plastic constitutive model known as Cvisc within the FLAC3D software. The Cvisc model in FLAC3D exhibits a visco-elastoplastic behavior in terms of both deviatoric and volumetric response. It is assumed that the visco-elastic and plastic strain-rate components act sequentially. Specifically, the visco-elastic constitutive law follows the Burgers model, consisting of a Kelvin unit connected in series with a Maxwell component, while the plastic constitutive law incorporates the Mohr-Coulomb model. For the sake of consistency within this section, the symbols s_{ij} and e_{ij} are employed to represent the deviatoric stress and strain components, respectively.

$$s_{ij} = \sigma_{ij} - \sigma_0 \delta_{ij} \qquad \text{Eq.2}$$

$$e_{ij} = \varepsilon_{ij} - \frac{e_{vol}}{3}\delta_{ij} \qquad \text{Eq.3}$$

Where:

$$\sigma_0 = \frac{\sigma_{kk}}{3} \qquad \text{Eq.4}$$

And

$$e_{vol} = \varepsilon_{kk} \qquad \text{Eq.4}$$

٢٦٤ Also, Kelvin, Maxwell, and plastic contributions to stresses and strains are labeled
٢٦٥ using *K*, *M*, and *P*, respectively. Strain rate partitioning:

$$\dot{e}_{ij} = \dot{e}_{ij}^{K} + \dot{e}_{ij}^{M} + \dot{e}_{ij}^{p} \qquad \text{Eq.5}$$

٢٦٦ Kelvin:

$$S_{ij} = 2\eta^{K}\,\dot{e}_{ij}^{K} + 2G^{K}\,\dot{e}_{ij}^{K} \qquad \text{Eq.6}$$

٢٦٧ Maxwell:

$$\dot{e}_{ij}^{M} = \frac{\dot{S}_{ij}}{2G^{M}} + \frac{S_{ij}}{2\eta^{M}} \qquad \text{Eq.7}$$

٢٦٨ Mohr-Coulomb:

$$\dot{e}_{ij}^{p} = \lambda^{*}\frac{\partial g}{\partial \sigma_{ij}} - \frac{1}{3}\dot{e}_{vol}^{p}\,\delta_{ij} \qquad \text{Eq.8}$$

$$\dot{e}_{vol}^{p} = \lambda^{*}\left[\frac{\partial g}{\partial \sigma_{11}} + \frac{\partial g}{\partial \sigma_{22}} + \frac{\partial g}{\partial \sigma_{33}}\right] \qquad \text{Eq.9}$$

٢٦٩ In turn, the volumetric behavior is given by

$$\dot{\sigma}_{0} = K\left(\dot{e}_{vol} - \dot{e}_{vol}^{p}\right) \qquad \text{Eq.10}$$

٢٧٠ Within these equations, the parameters *K* and *G* represent the bulk modulus and shear
٢٧١ modulus, respectively, while η denotes the dynamic viscosity (obtained by multiplying
٢٧٢ the kinematic viscosity with mass density). The Mohr-Coulomb yield envelope
٢٧٣ incorporates both shear and tensile conditions. The yield criterion is defined as $f = 0$,
٢٧٤ wherein the principal axes formulation yields the following: Shear yielding:

$$f = \sigma_{1} - \sigma_{3}N_{\varphi} + 2C \qquad \text{Eq.11}$$

٢٧٥ Tension yielding:

$$f = \sigma^t - \sigma_3 \qquad \text{Eq.12}$$

Where C is the material cohesion, φ is the friction, $N_\varphi = \frac{1+sin\varphi}{(1-sin\varphi)}$, σ^t is the tensile strength, and σ_1 and σ_3 are the minimum and maximum principal stresses (compression negative).

Shear failure:

$$g = \sigma_1 - \sigma_3 N_\psi \qquad \text{Eq.13}$$

Tension failure:

$$g = -\sigma_3 \qquad \text{Eq.14}$$

Where ψ is the material dilation and $N_\psi = \frac{1+sin\psi}{(1-sin\psi)}$. Finally, λ^* is a nonzero parameter during plastic flow only, which is determined by applying the plastic yield condition $f = 0$.

The main parameters of described creep model are Bulk modulus (K) (Elastic volumetric response – no creep), Kelvin viscosity(η^K), Kelvin shear modulus(G^K), Maxwell viscosity(η^M), Maxwell shear modulus (G^K), Cohesion (C), Angle of friction (φ), Angle of dilation (Ψ).

Particle breakage (PSD, particle breakage, rotation, and re-arrangement) of rock-fill particles over time, due to forming micro-cracks and changes in moisture content, are the main cause of creep deformation in these materials. These phenomena cause changes in the strength properties and deformability of these materials. Due to the anisotropic creep properties of rock-fill materials, large-scale accurate testing that can determine the main creep properties of rock-fill materials is so complex and expensive.

This creep test has not been performed on the rock-fill materials of Masjed-e-Soleyman Dam. Therefore, in this study, the creep model parameters are determined based on the results of triaxial tests and analysis trials. Table 4 shows the determined parameters.

The parameters of cohesion (C), friction angle (φ), and dilation angle (Ψ) are determined directly based on the results of triaxial tests (Table 2). With the help of parameters (K, n, v) in Table 2, the bulk modulus (K) and Maxwell shear modulus (G^M), were determined (Using Eq. 5 in appendix, $G^M=E/2(1+v)$, $K=E/3(1-2v)$) .The other values of creep parameters are determined based on analysis trials. Surface displacements and long-term settlement of survey measurement points (SMP) located between 0.8 and 0.6 of the dam heights from the crest axis (SMP23 in Fig. 2-Supplementary) have been selected for determining these creep parameters.

5. Sequence and calibration of modeling

The construction of the dam was completed in November 2000, following a period of approximately five years. Forty-two layers were employed in the simulation to replicate the placement process. The initial filling of the reservoir commenced one month after the completion of construction. During the initial filling, the water level in the reservoir was set at +255. The simulation accounts for impounding effects and collapse settlement, as discussed by Akhtarpour and Salari (2020) [2] and Mahin Roosta et al. (2012) [27]. Mahin Roosta and Alizadeh (2012) [27] proposed a stress reduction coefficient to mitigate the effective compressive stress components in the recently saturated layer. The influence of confining pressure on the collapse phenomenon [40], as well as the stress reduction coefficient (Cc) derived from trial analyses for each impounding stage, has been observed by several researchers (refer to Table 5).

After modeling the initial impounding, the constitutive model for the dam shell material was updated to include the Cvisc creep model, allowing the simulation of long-term

deformation by accounting for creep phenomena in the rock-fill shell materials and consolidation in the core. The simulation results showed a strong correlation between calculated pore pressure values and deformation patterns in the dam and the actual measured data from the central cross-section. This alignment between the simulated and observed values demonstrates the model's effectiveness in accurately replicating the dam's long-term behavior under creep and consolidation conditions. (See Fig. 4–Supplementary to 8–Supplementary)

6. Numerical Results and discussion

The pore pressure contours in CH.260 reveal that excess pore pressure did not develop in the upper portions of the core, while high excess pore pressure was observed in the lower sections due to the core's low permeability and high construction rate. At the lower levels, a nearly constant excess pore pressure was maintained between the core's center and upstream or downstream locations. Fig. 7, showing pore water pressure at September 2016, highlights the persistent high excess pore pressure in these lower areas, indicating the slow dissipation of pressure over time. (For details on pore pressure at the end of construction and the end of the first impounding, please refer to Fig. 9-Supplementary and 10-Supplementary.)

During the initial impounding, the core experienced nearly undrained conditions, leading to negligible dissipation of pore pressure from the end of the first impounding until the end of the analysis. The slow dissipation of excess pore pressure and high generation of pore water pressure in the lower part of the core created a quasi-fluid zone with zero effective stress. Effective vertical stresses decreased during impounding due to buoyancy forces in the upstream shell. The undrained nature of the core caused an increase in total stress due to water pressure on the upstream side, reducing the size of regions with zero effective stress near the upstream. Fourteen years after the first

impounding, a slight decrease in excess pore pressure led to an increase in effective stress, reducing the extent of the zero effective stress zone compared to earlier phases. Fig. 8, which shows pore water pressure at September 2016, illustrates this behavior clearly. (Refer to Fig. 11-Supplementary and 12- Supplementary for stress data at earlier stages.)

At the end of the first impounding, shear strain contours in the central cross-section indicated the generation of shear zones due to the placement of the embankment's upper parts. These zones further developed as a result of differential deformations between the upstream shell and core, along with water pressure effects on the core. Increased shear strain in the upstream core led to the formation of hydraulic cracks and contractive behavior, causing a rise in pore water pressure. During long-term creep deformation, particularly lateral creep towards the outer body, additional space was created for the core to deform in both directions, resulting in pronounced plastic shear deformations.

Additionally, principal stresses in the central cross-section at the end of the first impounding showed significant rotation due to oblique shear zones, with similar stress magnitudes observed near the filter regions and central core. This stress behavior underscores the complex interactions within the dam structure during and after impounding.

The upper sections of the dam adjacent to the abutments experience tensile stress, resulting in the development of transverse tensile cracks (Fig. 9). The extent of these tensile areas corresponds to the observed cracks on the crest. Based on the modeling results in September 2016, the maximum depth of the area with tensile stress in the core next to the right and left supports is 4.5 and 6 meters, respectively, relative to the crest level. Therefore, an important long-term issue that may affect the dam's safety is the

increasing depth of tension cracks in the core near the valley walls. This could potentially lead to internal erosion due to reservoir water leakage into these areas.

Vertical and horizontal displacements, along with the deformed mesh in the central cross-section at the completion of construction, show that settlement from consolidation was negligible due to the slow accumulation of excess pore pressure and the high excess pore pressure in the dam's lower regions during construction. Settlements in the shell were primarily influenced by variations in particle size distribution, breakage, rotation, and re-arrangement. Lateral deformations were also noted in the lower sections of the dam body, driven by oblique shear zones. (Refer to Fig. 13-Supplementary to 15-Supplementary)

Figs. 10-11 depict the outcomes of the end of the first impounding, showcasing the vertical and horizontal displacements. The maximum vertical displacement within the dam reaches 5.93 meters, while displacement at the crest is measured at 2.2 meters. Differential settlements are particularly noticeable at the upper regions of the interface between the shell and core on the upstream side. Water pressure on the upstream face contributes to smaller lateral deformations in the lower sections of the core compared to those observed during construction. A berm-like subsidence is evident in the upper portions of the upstream side of the dam, consistent with on-site observations. These collapse settlements in the upstream rock-fill shell are identified as the primary cause of the observed deformation behavior during the first impounding phase. The contour distribution of settlement and horizontal deformation within the central cross-section at the end of the first impounding in September 2016 is depicted in Figs. 12 and 13. Furthermore, Figs. 14 to 16 exhibit the contour distribution of settlement, horizontal deformation perpendicular to the dam axis, and horizontal deformation parallel to the dam axis on the three-dimensional model surface after the first impounding phase.

During the period from the end of impounding to September 2016, the maximum settlement of the dam crest is 3.1 meters, primarily occurring in the middle sections of the crest. The maximum horizontal deformation perpendicular to the dam axis is 1.9 meters, which is supported by field data and evidence. Throughout this period, the overall deformation behavior of the dam shells is directed towards the outer areas. However, the upper levels of the upper shell exhibit downward deformation, contrary to the lower levels. This deformation pattern results in a berm-like deformation complication in the upper sections upstream of the dam, aligning with field observations. The lower parts of the core experience lateral deformation towards the shells (bulging) due to the horizontal movements of the shell, while the upper parts of the core and shell subside. Furthermore, the geometric shape of the valley influences horizontal deformation towards the middle sections of the valley.

Fig. 17 depicts the deformed mesh of the main section of the dam, while Fig. 18 provides a three-dimensional view of the deformed mesh in September 2016 relative to the end of the first impounding. These figures reveal complications such as berm-like deformation on the upstream surface of the dam, core bulging at lower levels, and significant settlement in the middle parts of the dam crest.

Based on the aforementioned explanations, it can be concluded that the general mechanism behind the long-term deformation behavior of the MES dam is as follows: "The significant pore pressure generated in the core, coupled with the low permeability of the materials, results in almost undrained conditions in the lower levels of the dam core. The rock-fill materials in the dam shells possess a high potential for particle crushing, leading to substantial creep deformations over time. The creep deformations of the shell material towards the outer areas of the dam cause lateral deformation of the lower parts of the core towards the shells. The deformation behavior of the core at the

lower levels, under constant volume conditions and the formation of shear zones, causes simultaneous settlement in the upper sections of both the body and the core."

Fig. 19 illustrates the complex deformation mechanisms in the dam, highlighting settlement, creep, shear, and bulging effects. Settlement in the upper regions results from material compaction and consolidation under sustained loads. Creep deformation, shown by yellow arrows, represents the time-dependent lateral and vertical movements in the rock-fill shell, driven by stress conditions and environmental factors. A zero effective stress region within the core, marked by an outlined oval, exhibits quasi-fluid behavior due to high pore water pressure, contributing to ongoing deformation. Shear zones indicated by red lines show differential movements between the core and shell, leading to potential cracking and hydraulic fracturing. Bulging directions in the core, depicted by blue arrows, indicate outward deformation under lateral stresses.

7. Conclusions

This research aims to explain the long-term deformation behavior of the MES dam from the end of impounding to September 2016. Data from instruments and a mechanical-fluid three-dimensional numerical model were used to analyze the factors influencing deformation behavior. The key findings are as follows:

1) Excess pore pressure dissipates slowly during this period, resulting in minimal settlement from consolidation. The lower parts of the core exhibit nearly incompressible behavior.
2) Deformations in the rockfill dam, as observed through surface mapping points, micro-geodetic points in the underground gallery, and deviation meter measurements inside the downstream shell, have a negligible impact on long-term deformation behavior.
3) The creep behavior of rock-fill shell materials significantly contributes to the

deformation behavior of the dam during this period. Creep deformations in the shell material perpendicular to the dam's axis cause lateral deformation (bulging) in the lower regions of the core. The almost incompressible and undrained behavior of the lower parts of the core leads to settlement in the upper parts of the core and shells. This hypothesis provides a strong explanation for the mechanism of dam deformation behavior in the long term (see Fig. 19). The majority of settlement occurs on the dam crest, while surface deformation perpendicular to the dam's axis is most pronounced on the downstream shell.

4) The deformation mechanism results in upward movement of the upper parts of the upstream shell and downward movement of the lower parts, leading to a berm-like complication in the upper levels of the upstream shell.

5) The dam body experiences horizontal deformation towards the middle sections due to significant settlement in the central cross-section. This results in areas with tensile stresses adjacent to the valley walls. Based on modeling results in September 2016, the maximum depth of the area with tensile stress in the core adjacent to the right and left abutments is 4.5 and 6 meters relative to the crest level, respectively.

6) This study confirms that the phenomenon of creep deformation in the used materials of rockfill, such as those used in tall structures like rockfill dams, can play a determining role in the long-term deformation behavior of these structures. Additionally, the creation and development of significant excess pore pressure in the clay core of tall rockfill dams can be another major influential factor in these particular megastructures.

Currently, there is no evidence of a significant reduction in the deformation rate of the Masjed-e-Soleyman dam, and these deformations due to the creep phenomenon in the

rock-fill shell material may continue with the proposed mechanism for several decades after dewatering. In these conditions, one of the issues that may affect the long-term safety of the dam is the increase in the depth of tension cracks in the core of the dam in areas adjacent to the valley walls. With the penetration of reservoir water into these areas, the occurrence of internal erosion is likely. Another risk that can affect the dam's safety is the reduction in height due to significant settlement on the dam crest.

However, predicting the deformation behavior of the dam in the future, with the proposed deformation mechanism in this article, can become the subject of future studies and research by identifying hazards and destabilizing factors of the dam, as well as providing remedial solutions.

Appendix : Mechanical Constitutive model

A numerical simulation was conducted using FLAC3D software to analyze the mechanical behavior of the dam's materials. The simulation utilized an elasto-plastic hardening/softening constitutive model based on the Mohr-Coulomb model. This model accurately captures the initial elastic response of the materials by incorporating Young's modulus (E) and Poisson's ratio (υ). Subsequently, the model accounts for the hardening/softening and dilative behavior of the materials by considering parameters such as friction angle, cohesion, dilation angle, and tensile strength as functions of plastic shear strain and tensile strain, until they reach their maximum values.

Yield envelopes and potential functions

The yield surface functions of this constitutive model were mathematically defined by Eqs. (1) and (2).

$$f^s = \sigma_1 - \sigma_3 \frac{1-\sin\phi_m}{1+\sin\phi_m} + 2c_m \sqrt{\frac{1-\sin\phi_m}{1+\sin\phi_m}} \qquad \text{Eq. 1}$$

$$f^t = \sigma_m^t - \sigma_3 \qquad \text{Eq. 2}$$

In the following set of equations, the variables f^s and f^t denote the shear and tensile yield functions, respectively. The variables σ_1 and σ_3 represent the maximum and minimum principal stresses. Additionally, ϕ_m, c_m and σ_m^t signify the mobilized friction angle, mobilized cohesion, and mobilized tensile strength of the model, respectively.

The non-associated flow rule was adopted for shearing, while the associated flow rule was employed for tension. The plastic potential functions were defined as follows:

$$Q^S = \sigma_1 - \sigma_3 \frac{1-\sin\psi_m}{1+\sin\psi_m} \qquad \text{Eq. 3}$$

$$Q^t = -\sigma_3 \qquad \text{Eq. 4}$$

In the presented set of equations, we introduce the variables Q^S and Q^t, which represent the shear and tensile plastic potential functions, respectively. Furthermore, ψ_m denotes the mobilized dilation angle.

Stress-dependent elastic modulus

In the majority of geotechnical materials, it is observed that the elastic modulus is influenced by the confining stress. Consequently, to account for this dependency, Equation (5) proposed by Duncan and Chang (1970) in their hyperbolic (nonlinear elastic) model is incorporated into the constitutive model. This equation serves to define and represent the relationship between the elastic modulus and the confining stress.

$$E = KP_a\left(\frac{\sigma_3}{P_a}\right)^n \qquad \text{Eq. 5}$$

The equation presented herein introduces various parameters related to the elastic behavior of materials in civil engineering. In this context, E represents Young's modulus, K denotes the elastic modulus, Pa signifies the atmospheric pressure, and n represents the exponent governing the dependence of the elastic modulus on the confining stress. Furthermore, the Poisson's ratio (υ) is considered as a constant value in this study. The combination of these elasticity parameters ensures an appropriate response within the elastic domain of the constitutive model.

Frictional hardening

Vermeer and de Borst (1984) [37] put forward a formulation describing the frictional hardening behavior of geotechnical materials. This formulation accounts for the variation of the mobilized friction angle, denoted as ϕ_m, with respect to the plastic shear strain, exhibiting a gradual increase towards its peak value ϕ_p. Building upon this work, Mahinroosta et al. (2015) [28] introduced a

modification to the aforementioned relation by considering an initial mobilized friction angle, ϕ_0.

The resulting modified equation is presented below:

$$\sin\phi_m = \begin{cases} \sin\phi_0 + 2\dfrac{\sqrt{\varepsilon_s^p \times \varepsilon_s^f}}{\varepsilon_s^p + \varepsilon_s^f}(\sin\phi_p - \sin\phi_0) & for\ \varepsilon_s^p \le \varepsilon_s^f \\ \sin\phi_p & for\ \varepsilon_s^p > \varepsilon_s^f \end{cases} \quad \text{Eq. 6}$$

Within the given equation, the plastic shear strain is represented by ε_s^p, while ε_s^f denotes the plastic shear strain at the peak friction angle. An important parameter, denoted as ϕ_0, plays a significant role in determining the range of elastic behavior that materials exhibit. This parameter is known to be influenced by the confining stress and can be defined as a function thereof.

Dilatancy behavior

In the field of geotechnical engineering, Rowe (1963) [38] put forward Eq. 7 to explain the phenomenon of dilatancy hardening exhibited by geotechnical materials.

$$\sin\psi_m = \frac{\sin\phi_m - \sin\phi_{cv}}{1 - \sin\phi_m \sin\phi_{cv}} \quad \text{Eq.7}$$

In the context of civil engineering, the parameter ψ_m represents the mobilized dilation angle, while ϕ_{cv} corresponds to the critical state friction angle or the friction angle of constant volume. This critical state friction angle value can be determined by utilizing Eq. 8.

$$\sin\phi_{cv} = \frac{\sin\phi_p - \sin\psi_p}{1 - \sin\phi_p \sin\psi_p} \quad \text{Eq. 8}$$

In the realm of civil engineering, the peak dilation angle denoted as ψ_p assumes significance. To refine Rowe's stress-dilatancy equation for rockfill material, formulation is simplified and revised as presented below:

$$\sin\psi_m = R_d \frac{\sin\phi_m - \sin\phi_{cv}}{1 - \sin\phi_m \sin\phi_{cv}} \quad \text{Eq. 9}$$

In the aforementioned equation, R_d is incorporated as a reduction factor with a value less than one,

representing the influence of particle size distribution (PSD), particle breakage, rotation, and rearrangement on the deformation behavior of rockfill material. In their recent study, Akhtapour and Salari (2020) [2] introduced Eq. 10 as a more comprehensive alternative to Eqs. 7 and 9.

$$\sin\psi_m = \begin{cases} \sin(I_c.\psi_{mR}) & -90 \le I_C.\psi_{mR} \le 0 \\ \sin(R_d.\psi_{mR}) & 0 < R_d.\psi_{mR} \le 90 \end{cases} \quad \text{Eq. 10}$$

In the aforementioned equation, ψ_{mR} represents the mobilized dilation angle acquired through the utilization of Rowe's equation, expressed in degrees. I_c denotes the contraction factor, a value exceeding zero and potentially surpassing unity. This factor serves as an appropriate metric for quantitatively evaluating the magnitude of the influences exerted by PSD, particle breakage, rotation, and rearrangement on the deformation of rockfill materials throughout the contraction phase.

Stress dependent peak friction and dilation angle

The experimental analysis conducted in the laboratory has revealed that the ultimate friction angles are influenced by the applied confining pressure. Consequently, this interrelation is taken into consideration in the constitutive model through the implementation of Eq. 11. The stress-responsive friction angle, as determined, is utilized as the upper limit for friction in Eq. 8.

$$\phi_p = \phi_s - \Delta\phi \log(\frac{\sigma_3}{P_a}) \quad \text{Eq. 11}$$

In the aforementioned equation, ϕ_p represents the utmost friction angle, σ_3 denotes the minor principal stress, and ϕ_s signifies the internal friction angle at $\sigma_3 = 100kPa$. Pa corresponds to the atmospheric pressure, while $\Delta\phi$ represents the decrement in friction angle with respect to the confining pressure for every tenfold increment in σ_3 .

In the realm of geotechnical materials, the maximum dilation angle, denoted as ψ_p , is contingent

upon the applied confining pressure. In a general sense, the peak dilation angle, ψ_p, exhibits a diminishing trend as the confining pressure, σ_3, experiences an augmentation.

The supplementary data is available at:

file:///C:/Users/pc/Downloads/Supplementary-file.pdf

References

1. Pinyol, N. and Alonso, E. "Design, construction, monitoring and modelling of Albagés Earth Dam: A case history", Int. J. Civ. Eng., 17(3), pp. 501–513 (2019). DOI: 10.1007/s40999-018-0314-z
2. Aktarpour, A. and Salari, M. "The deformation mechanism of a high rockfill dam during the construction and first impounding", Scientia Iranica, 17(2), pp. 566-587 (2020). DOI: 10.24200/sci.2018.20778
3. Feng, S., Wang, W., Hu, W., Deng, Y., Yang, J., Wu, S., Zhang, C. and Hoeg, K. "Design and performance of the Quxue asphalt-core rockfill dam", Soils and Foundations, 60(4), pp. 1036-1049 (2020). DOI: 10.1016/j.sandf.2020.06.008
4. Wang, L., Wu, C., Tang, L. et al. "Efficient reliability analysis of earth dam slope stability using extreme gradient boosting method", Acta Geotech., 15(2), pp. 3135–3150 (2020). DOI: 10.1007/s11440-020-00962-4
5. Wang, L., Wu, C., Gu, X. et al. "Probabilistic stability analysis of earth dam slope under transient seepage using multivariate adaptive regression splines", Bull. Eng. Geol. Environ., 79(3), pp. 2763–2775 (2020). DOI: 10.1007/s10064-020-01730-0
6. Liu, S., He, W., Sun, Y., Shen, C. and Wang, L. "Analysis of the behavior of a high earth-core

rockfill dam considering particle breakage", Computers and Geotechnics, 157(2), p. 105320 (2023). DOI: 10.1016/j.compgeo.2023.105320

7. Alemie, N.A., Wosenie, M.D., Belew, A.Z., Kibret, E.A. and Ayele, W.T. "Performance evaluation of asphalt concrete core earth-rock fill dam relative to clay core earth-rock fill dam in the case of Megech Dam, Ethiopia", Arabian Journal of Geosciences, 14(24), p. 2712 (2021). DOI: 10.1007/s12517-021-09009-8
8. Zhang, W., Wu, J.H., Gu, X. et al. "Probabilistic stability analysis of embankment slopes considering the spatial variability of soil properties and seismic randomness", J. Mt. Sci., 19(4), pp. 1464–1474 (2022). DOI: 10.1007/s11629-021-6981-2
9. Pan, J., Jiang, J., Cheng, Z., Xu, H. and Zuo, Y. "Large-scale true triaxial test on stress-strain and strength properties of rockfill", International Journal of Geomechanics, 20(1), p. 04019146 (2020). DOI: 10.1061/(ASCE)GM.1943-5622.0001527
10. Han, H., Li, J., Shi, J. and Yang, C. "Influence of scale effect on strength and deformation characteristics of rockfill materials", Materials, 15(15), p. 5467 (2022). DOI: 10.3390/ma15155467
11. Guo, Y., Chi, S., Mi, X. and Yan, S. "Experimental investigation of statistical characteristics of elastic mechanical parameters and strength indexes of rockfill particles", Granular Matter, 25(2), p. 30 (2023). DOI: 10.1007/s10035-022-01302-x
12. Duncan, J. and Chang, C. "Nonlinear analysis of stress and strain in soils", J. Soil Mech. Found. Div. ASCE, 96(5), pp. 1629-1653 (1970). DOI: 10.1061/JSFEAQ.0001458
13. Shen, C., Liu, S. and Wang, L. "Elasto-plastic constitutive modelling of compacted rockfill materials: a physically based approach", Géotechnique, 71(4), pp. 1-13 (2021). DOI: 10.1680/jgeot.21.00100

14. Guo, R. and Li, G. "Elasto-plastic constitutive model for geotechnical materials with strain-softening behavior", Comput. Geotech., 34(1), pp. 14–23 (2008). DOI: 10.1016/j.cageo.2007.03.012
15. Escuder, I., Andreu, J. and Reche, M. "An analysis of stress-strain behaviour and wetting effects on quarried rock shells", Can. Geotech. J., 42(1), pp. 51–60 (2005). DOI: 10.1139/t04-071
16. Vasistha, Y., Gupta, A.K. and Kanwar, V. "Medium triaxial testing of some rockfill materials", J. Geotech. Eng., 18(4), pp. 923–964 (2013).
17. Kalantary, F., Sadoghi Yazdi, J. and Bazazzadeh, H. "Validation and application of evolutionary computational technique on disturbed state constitutive model", Int. J. Civ. Eng., 12(3), pp. 216-225 (2014). URL: http://ijce.iust.ac.ir/article-1-845-en.html
18. Naylor, D.J. "Collapse settlement–Some developments", In Applications of Computational Mechanics in Geotechnical Engineering, pp. 37-54 (2020). ISBN: 9781003078111
19. Alonso, E.E. and Oldecop, L.A. "Fundamentals of rockfill collapse", Unsaturated Soils for Asia, pp. 3-13 (2020). ISBN: 9781003078616
20. Ventini, R., Flora, A., Lirer, S., Mancuso, C. and Cammarota, A. "An experimental study of the behaviour of two rockfills accounting for the effects of degree of saturation", EDP Sciences, 195(3), p. 03033 (2020). DOI: 10.1051/e3sconf/202019503033
21. Wu, Y., Yin, Y., Zhang, B., Sun, X. and Yu, Y. "Unsaturated wetting deformation characteristics of a granite rockfill under rainfall conditions", Canadian Geotechnical Journal, 59(10), pp. 1774-1792 (2022). DOI: 10.1139/cgj-2021-0047
22. Zhou, X., He, J., Chi, S. and Wang, J. "Study on collapse settlement and cracks of core wall rockfill dams under wetting deformation", International Journal for Numerical and Analytical

٦٢١ Methods in Geomechanics, 47(1), pp. 106-128 (2023). DOI: 10.1002/nag.3462
٦٢٢ 23. Cheng, J., Ma, G., Zhang, G., Wang, Q. and Zhou, W. "Deterioration of mechanical properties
٦٢٣ of rockfill materials subjected to cyclic wetting–drying and wetting", Rock Mechanics and
٦٢٤ Rock Engineering, 56(4), pp. 2633-2647 (2023). DOI: 10.1007/s00603-022-03209-8
٦٢٥ 24. Hunter, G. "The pre- and post-failure deformation behaviour of soil slopes", (PhD Thesis),
٦٢٦ University of New South Wales, Australia (2003). DOI: 10.26190/unsworks/20980
٦٢٧ 25. Naylor, D., Maranha das Neves, E., Mattar, J. and Veiga Pinto, A. "Prediction of construction
٦٢٨ performance of Beliche Dam", Géotechnique, 36(3), pp. 359–376 (1986). DOI:
٦٢٩ 10.1680/geot.1986.36.3.359
٦٣٠ 26. Oldecop, L. and Alonso, E. "Suction effects on rockfill compressibility", Géotechnique, 53(2),
٦٣١ pp. 289-292 (2003). DOI: 10.1680/geot.2003.53.2.289
٦٣٢ 27. Mahin Roosta, R. and Alizadeh, A. "Simulation of collapse settlement in rockfill material due
٦٣٣ to saturation", Int. J. Civ. Eng., 10(2), pp. 93-99 (2012). URL: http://ijce.iust.ac.ir/article-1-
٦٣٤ 521-en.html
٦٣٥ 28. Mahinroosta, R., Aliadeh, A. and Gatmiri, B. "Simulation of collapse settlement of first filling
٦٣٦ in a high rockfill dam", Engineering Geology, 187(2), pp. 32-44 (2015). DOI:
٦٣٧ 10.1016/j.enggeo.2014.12.013
٦٣٨ 29. Charles, J. "Geotechnical properties of coarse-grained soils", Proc. of the 12th Int. Conf. on
٦٣٩ Soil Mechanics and Foundation Engineering, General Report, Discussion Session 8, pp. 2495–
٦٤٠ 2519 (1989).
٦٤١ 30. Oldecop, L. and Alonso, E.E. "Fundamentals of rockfill time-dependent behaviour", Proc. 3rd
٦٤٢ Int. Conf. on Unsaturated Soils, Recife, 2(1), pp. 793–798 (2002).
٦٤٣ 31. Osses, R., Majdanishabestari, K., Ovalle, C. and Pineda, J. "Testing and modelling total suction

effects on compressibility and creep of crushable granular material", Soils and Foundations, 61(6), pp. 1581-1596 (2021). DOI: 10.1016/j.sandf.2021.09.006

32. Xu, M., Jin, D. and Zhou, W. "An experimental study on the time-dependent behavior of crushable granular materials using 3D-printed particles", Acta Geotechnica, 17(1), pp. 93-104 (2022). DOI: 10.1007/s11440-021-01232-7

33. Zhou, X., Shen, F. and Berto, F. "Experimental study on triaxial creep behavior of red sandstone under different pore pressures based on ultrasonic measurement", Fatigue & Fracture of Engineering Materials & Structures, 45(8), pp. 2388-2402 (2022a). DOI: 10.1111/ffe.13753

34. Zhou, X., Pan, X. and Berto, F. "A state-of-the-art review on creep damage mechanics of rocks", Fatigue & Fracture of Engineering Materials & Structures, 45(3), pp. 627-652 (2022b). DOI: 10.1111/ffe.13625

35. Bauer, E. "Constitutive modelling of wetting deformation of rockfill materials", Int. J. Civ. Eng., 17(1), pp. 481-486 (2019). DOI: 10.1007/s40999-018-0327-7

36. Nobari, E. and Duncan, J. "Effect of reservoir filling on stresses and movements in earth and rockfill dams", Report TE-72, University of California, Department of Civil Engineering (1972).

37. Vermeer, P. and De Borst, R. "Non-associated plasticity for soils, concrete and rock", Heron, 29(3), pp. 12-27 (1984). URL: https://resolver.tudelft.nl/uuid:4ee188ab-8ce0-4df3-adf5-9010ebfaabf0

38. Rowe, P. "Stress-dilatancy, earth pressure and slopes", J. Soil Mech. Found. Div. ASCE, 89(5), pp. 37-61 (1963). DOI: 10.1061/JSFEAQ.0000520

39. Itasca Consulting Group. "FLAC3D, User's manuals", Itasca Consulting Group, Minnesota

(2012).

40. Hasanzadehshooiili, H.M., Lakirouhani, A. and Oshtaghi, V. "Using artificial neural network (ANN) in prediction of collapse settlements of sandy gravels", Arab. J. Geosci., 7(6), pp. 2303–2314 (2014). DOI: 10.1007/s12517-013-0858-9

Figure Captions

Fig. 1. The variation of settlement of surface survey points on the dam body in the maximum cross-section from the end of the first impounding, during the long-term period

Fig. 2. The variation of horizontal displacements (perpendicular to the dam axis) of surface survey points on the dam body in the maximum cross-section from the end of the first impounding during the long-term period (a positive value means displacement toward upstream)

Fig. 3. Division of embankment for analysis of surface deformations during the post-construction period

Fig. 4. Settlements measured at the survey points installed in the lower gallery of the foundation

Fig. 5. Vertical profile of relative horizontal displacements in downstream inclinometers

Fig. 6. 3D numerical model and grid generation of the dam and foundation

Fig. 7. Pore water pressure (September 2016)

Fig. 8. Effective vertical stress (September 2016)

Fig. 9. Tensile stress (September 2016)

Fig. 10. relative settlement to the end of the first impounding (September 2016)

Fig. 11. Relative horizontal displacement to the end of first impounding (Septamter2016)

Fig. 12. Relative vertical displacement to the end of first impounding (September 2016)

Fig. 13. Relative horizontal displacement to the end of first impounding (September 2016)

Fig. 14. Relative surface settlement to the end of first impounding (September 2016)

Fig. 15. Relative surface horizontal displacement to the end of first impounding (September 2016)

Fig. 16. Relative horizontal displacement parallel to the end of first impounding to axis dam (September 2016)

Fig. 17. Relative deformed mesh to the end of first impounding with scale 10:1 (September 2016)

Fig. 18. Relative deformed mesh to the end of first impounding with scale 10:1 (September 2016)

Fig. 19. Schematic sketch of long-term deformation mechanism of the dam

Table Captions

Table 1. Absolute pore water pressure ratio, r_u, and the ratio of total vertical stress to total horizontal stress, r_K, at the core in the instrumented main chainage

Table 2. different regions parameters of the embankment

Table 3. The rock mass parameters

Table 4. The parameters of the creep model for dam shell

Table 5. Data of different stages of impounding

Figure List

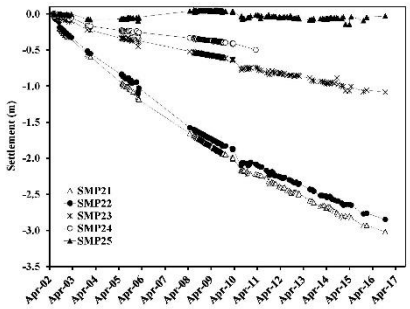

Fig. 1. The variation of settlement of surface survey points on the dam body in the maximum cross-section from the end of the first impounding, during the long-term period

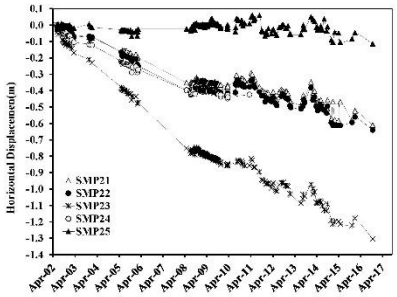

Fig. 2. The variation of horizontal displacements (perpendicular to the dam axis) of surface survey points on the dam body in the maximum cross-section from the end of the first impounding during the long-term period (a positive value means displacement toward upstream)

٧١٠

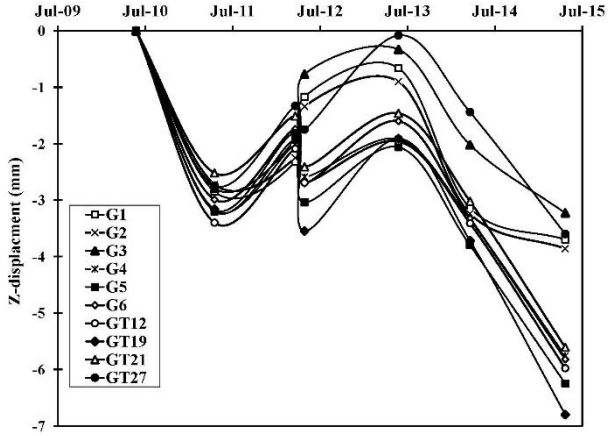

Fig. 4. Settlements measured at the survey points installed in the lower gallery of the foundation

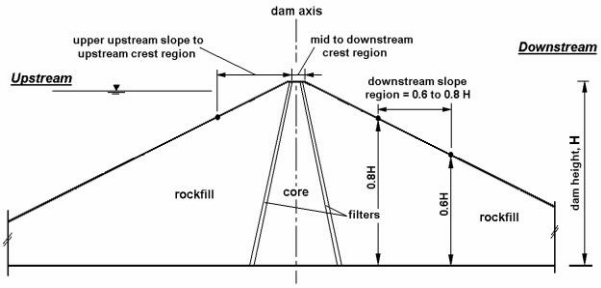

Fig. 3. Division of embankment for analysis of surface deformations during the post-construction period

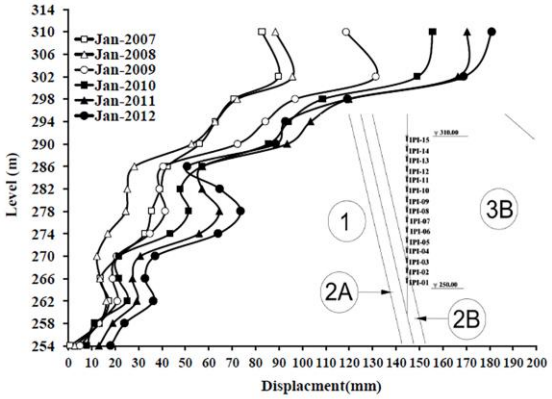

Fig. 5. Vertical profile of relative horizontal displacements in downstream inclinometers

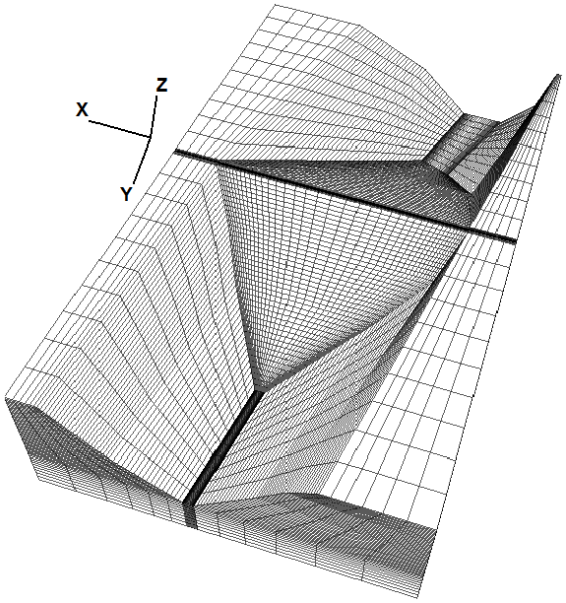

Fig. 6.3D numerical model and grid generation of the dam and foundation

٧١١

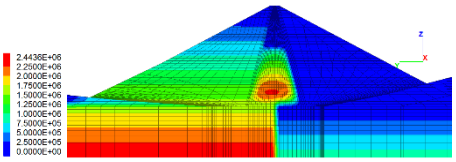

Fig. 7. Pore water pressure (September 2016)

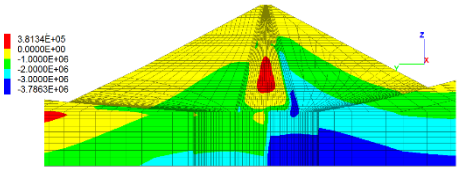

Fig. 8. Effective vertical stress (September 2016)

٧١٢

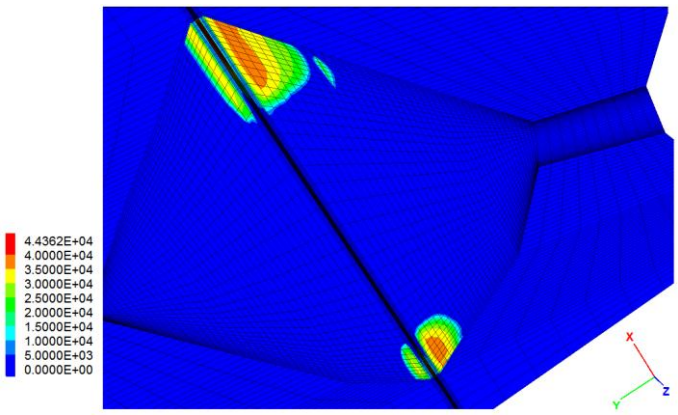

Fig. 9. Tensile stress (September 2016)

٧١٣

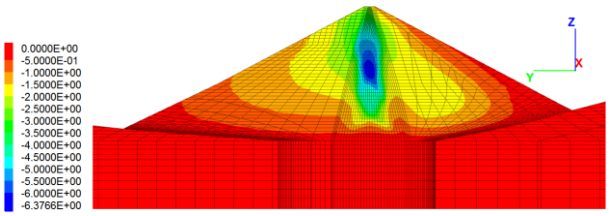

Fig. 10. relative settlement to the end of the first impounding (September 2016)

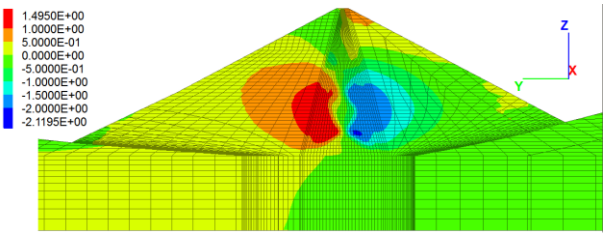

Fig. 11. Relative horizontal displacement to the end of first impounding (Septamter2016)

٧١٤

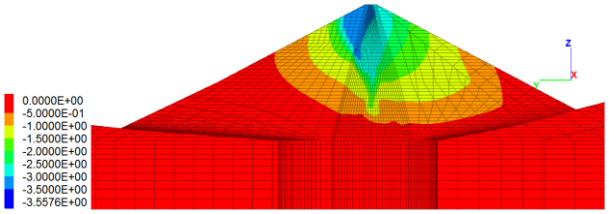

Fig. 12. Relative vertical displacement to the end of first impounding (September 2016)

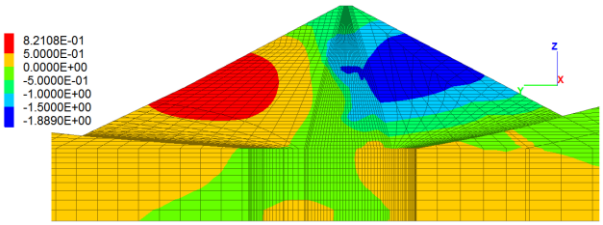

Fig. 13. Relative horizontal displacement to the end of first impounding (September 2016)

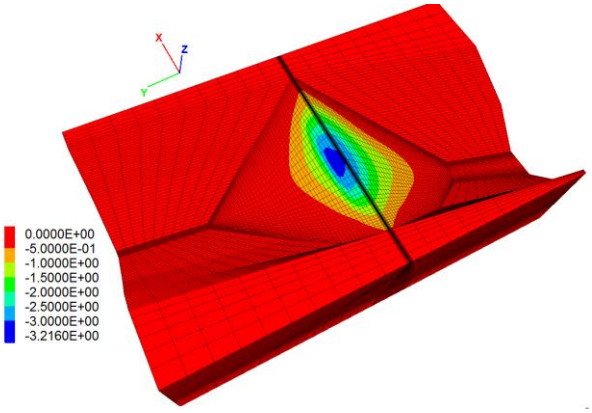

Fig. 14. Relative surface settlement to the end of first impounding (September 2016)

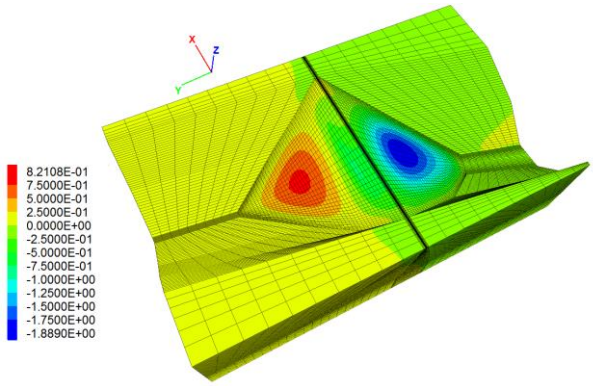

Fig. 15. Relative surface horizontal displacement to the end of first impounding (September 2016)

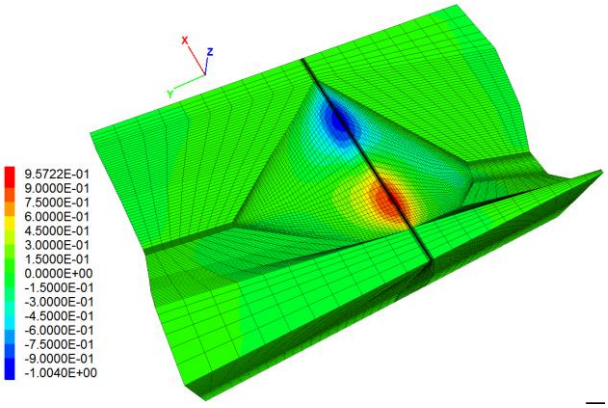

Fig. 16. Relative horizontal displacement parallel to the end of first impounding to axis dam (September 2016)

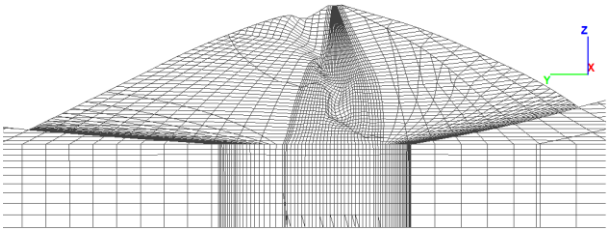

Fig. 17. Relative deformed mesh to the end of first impounding with scale 10:1 (September 2016)

٧١٥

٧١٦

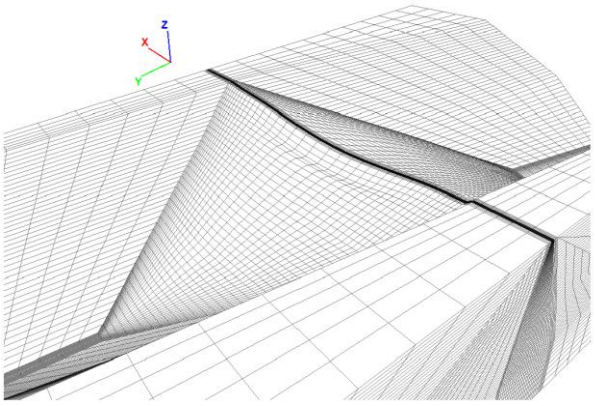

Fig. 18. Relative deformed mesh to the end of first impounding with scale 10:1 (September 2016)

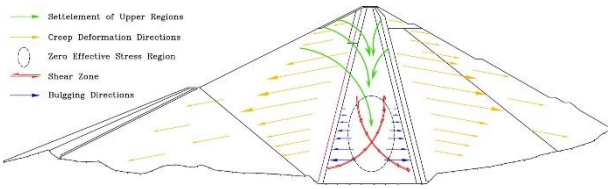

Fig. 19. Schematic sketch of long-term deformation mechanism of the dam

٧١٧ **Table List**

Table 1. Absolute pore water pressure ratio, r_u, and the ratio of total vertical stress to total horizontal stress, r_K, at the core in the instrumented main chainage

Loc.		2003	2004	2005	2006	2007	2008	2009	2010	2011	2012	2013	2014	2016
C1	r_k	1	1	0.99	0.98	0.97	0.96	0.95	-	-	-	-	-	-
	r_u	0.98	0.97	0.97	-	-	-	-	-	-	-	-	-	-
C2	r_k	0.74	0.74	0.73	0.69	0.69	-	-	-	-	-	-	-	-
	r_u	0.9	0.92	0.93	0.92	0.92	0.92	0.92	-	-	-	0.9	0.8٩	0.8٨
C3	r_k	1.03	1.02	-	-	-	-	-	-	-	-	-	-	-
	r_u	1.03	1.02	1.01	-	-	-	-	-	-	-	-	-	-
C4	r_k	1	1.01	1.03	1.05	1.08	1.05	1.07	-	-	-	-	-	-
	r_u	1.04	1.04	1.06	1.04	1.06	1.05	1.04	-	-	-	-	-	-
C5	r_k	-	-	-	-	-	-	-	-	-	-	-	-	-
	r_u	0.58	0.82	0.81	0.8	0.78	0.77	0.76	-	-	-	-	-	-
C6	r_k	1	1	0.99	0.98	0.97	0.96	0.95	-	-	-	-	-	-
	r_u	0.98	0.97	0.97	-	-	-	-	-	-	-	-	-	-

٧١٨

Table 2. The mechanical and flow parameters of the different regions of the embankment

Zone	3A,3C (Saturated)	3A,3C(dry)	3B	۲A	2B,2C	Core
$\rho_d(\frac{gr}{cm^3})$	2	2	2	1.9	2.1	1.89
n	0.74	-0.12	0.05	1	0	0.8
K	556	3672	422	138	1663	120
V	0.1	0.1	0.2	0.15	0.1	0.15
$C(\frac{kN}{m^2})$	25	65	40	10	20	30
$\varepsilon_f(\%)$	6	6	7	8.5	8.5	10
I_d	$0.77.(\frac{\sigma_3}{P_a})+0.25$	5	2.5	3.5	1	1
R_d	1	1	1	1	1	1
φ_P	$55-11.1\log(\frac{\sigma_3}{P_a})$	$51.3-7.\log(\frac{\sigma_3}{P_a})$	$42.23-0.64.\log(\frac{\sigma_3}{P_a})$	$45-6.64.\log(\frac{\sigma_3}{P_a})$	$46.36-4.82.\log(\frac{\sigma_3}{P_a})$	30
ψ_P	$\begin{cases}5.5 & \frac{\sigma_3}{P_a}\le 3\\ 0.0 & \frac{\sigma_3}{P_a}>3\end{cases}$	$\begin{cases}1.5 & \frac{\sigma_3}{P_a}\le 6\\ 0.0 & \frac{\sigma_3}{P_a}>6\end{cases}$	0	0	$1.15-0.83.\log(\frac{\sigma_3}{P_a})$	0
φ_0	$41.9-30.\log(\frac{\sigma_3}{P_a})$	$33.6-16.6.\log(\frac{\sigma_3}{P_a})$	$34.2-19.93.\log(\frac{\sigma_3}{P_a})$	$39.7-2.7.\log(\frac{\sigma_3}{P_a})$	$30-2.6.\log(\frac{\sigma_3}{P_a})$	0
K_{int} (cm/s)	1×10^{-1}	1×10^{-1}	1×10^{-4}	2×10^{-2}	1×10^{-2}	Eq.(1)

۷۱۹

Table 3. The rock mass parameters

Model	$\rho_d(\frac{gr}{cm^3})$	E(GPa)	ν	K_{int} (cm/s)
Linear elastic	2.4	2	0.25	5×10^{-8}

۷۲۰

۷۲۱

Table 4. The parameters of the creep model for dam shell

Parameter	3A,3C,dry	3A, saturated	3B
Bulk(K) G^M	With the help of parameters (K, n, v) in Table 2		
$C\ (\frac{kN}{m^2})$	65	25	40
Ψ	$\begin{cases} 1.5 & \frac{\sigma_3}{P_a} \le 6 \\ 0.0 & \frac{\sigma_3}{P_a} > 6 \end{cases}$	$\begin{cases} 5.5 & \frac{\sigma_3}{P_a} \le 3 \\ 0.0 & \frac{\sigma_3}{P_a} > 3 \end{cases}$	0
φ	$51.3 - 7.\log(\frac{\sigma_3}{P_a})$	$55 - 11.1\log(\frac{\sigma_3}{P_a})$	$42.23 - 0.64.\log(\frac{\sigma_3}{P_a})$
Tension$(\frac{kN}{m^2})$	0	0	0
G^K	Approximately, 10% of G^M		
η^K (GPa.s)	1×10^8	1.1×10^8	1.42×10^8
η^M (GPa.s)	2.5×10^6	2.9×10^6	3.3×10^6

٧٢٢

Table 5. Data of different stages of impounding

Stage of impounding	1	2	3	4	5	6
Range of reservoir water level (m)	255-288	288-312	312-328	328-335	335-357	357-371
Duration (day)	1	9	49	12	446	34
C_C	0.1	0.1	0.8	0.8	0.8	0.8

٧٢٣

٧٢٤

٧٢٥

٧٢٦ **First Author (Morteza Salari):**

٧٢٧ Morteza Salari has graduated in MSc of Geotechnical Engineering from Ferdowsi university of Mashhad
٧٢٨ in 2009. He is now an Expert in Maharab Consulting Engineering Company in Mashhad. Also, he has some

experiences on the field of embankment dam engineering for the 11 years. Also, he is a PhD student in Ferdowsi university of Mashhad.

Second Author (Ali Akhtarpour):

Dr Ali Akhtarpour was graduated from polytechnic university of Tehran in BSc of civil engineering, MSc (Under supervision of Dr Abbas Soroush) and PhD (Under supervision of Dr Ali Khodaii) of geotechnical engineering in 2000, 2003 and 2011 respectively. Now he is a staff member (Associate Prof.) of engineering faculty in the Ferdowsi University of Mashhad. Also he has some experiences on the embankment dam design, monitoring and numerical modelling for more than 20 years. You can find more about publications and interesting subject area in his personal homepage as below:

http://akhtarpour.profcms.um.ac.ir/

Third Author (Sajjad Khosravi):

Sajjad Khosravi is a geotechnical engineer with a Master's degree in Geotechnical Engineering from Iran University of Science and Technology. With over four years of research experience, he has recently concluded his role as a Research Assistant at Ferdowsi University of Mashhad. His areas of expertise include machine learning methods and numerical modeling in geotechnical engineering. He has also contributed to the design of two tunnel shield lines in Mashhad and authored multiple papers on machine learning and numerical modeling in geotechnical engineering.